CHAPTER 3

Application of Mesoscale Field-Based Models to Predict Stability of Particle Dispersions in Polymer Melts

Prasanna K. Jog[*,1], **Valeriy V. Ginzburg**[1], **Rakesh Srivastava**[1], **Jeffrey D. Weinhold**[2], **Shekhar Jain**[3], and **Walter G. Chapman**[4]

Contents

1 The Dow Chemical Company, Midland, MI 48674, USA
2 The Dow Chemical Company, Freeport, TX 77515, USA
3 Shell Technology India Pvt. Ltd., Bangalore 560048, India
4 Department of Chemical and Biomolecular Engineering, Rice University, Houston, TX 77005, USA

* Corresponding author.
E-mail address: PKJog@dow.com

Advances in Chemical Engineering, Volume 39
ISSN: 0065-2377, DOI 10.1016/S0065-2377(10)39003-X

Abstract We review recent results in theoretical modeling of particle dispersions in polymer melts. In particular, we focus on mesoscale field-based theories (interfacial statistical association fluid theory (iSAFT) and compressible self-consistent field theory (SCFT)). To demonstrate the application of these theories, we calculate "dispersion phase maps" for particles with grafted oligomer brushes mixed into polymer melts. The systems used here are generic and can be considered as model systems for a wide class of application areas. Examples include dispersion of nanoparticles in a polymer matrix and stabilization of polymer blends by addition of a block copolymer. It is demonstrated that, as expected, the quality of particle dispersion depends strongly on the brush grafting density and the ratio of the oligomer length to the matrix polymer length. The results obtained using two different methods (iSAFT and SCFT) show remarkable agreement for the case of the so-called "athermal" mixtures. Applying the analysis to the case of polymer–clay nanocomposites, we propose a new hypothesis for the ubiquity of the so-called "intercalated" morphologies. Overall, this example demonstrates the utility of mesoscale field-based models like iSAFT and SCFT for chemical engineering applications.

1. INTRODUCTION

The balance in modern chemical industry is gradually shifting from large integrated plants and commodity-based products to high-value specialty products involving micro- and nanostructured materials using advanced material science, high-throughput technology, and sophisticated computing tools. A common practice in making these specialty products is to disperse organic or inorganic particles in polymer melts to provide enhanced toughness, chemical resistance, or other desirable properties.

Applications of such materials range from performance polymers to pharmaceutical suspensions, agricultural and environmentally benign chemicals, microelectronics, and biological systems. Polymer adsorption is important to commercial applications such as inks, paints, and coatings, where there is considerable interest in understanding and controlling the segregation to the surface of one component from a blend of polymers. Water-soluble polymers acting as colloidal stabilizers are the enabling

component in the development of environment-friendly water-based coatings that replace older formulations employing organic solvents. Adsorption-based surface treatments comprise an inexpensive means of surface modification for DNA separations and recognition chips. Surface modification strategies that accommodate molecules with a complex distribution of hydrophobicity and charge will facilitate extensions to protein separations. Among the naturally occurring systems, the mechanical properties of biological cell membranes depend upon the fraction of cholesterol molecules and conformational degrees of freedom of the lipids forming the layer. Porous materials with pore sizes on the order of a few nanometers are widely used in chemical, oil and gas, food, and pharmaceutical industries for pollution control and mixture separation and as catalyst and catalyst supports for chemical reactions. The design of such processes is largely empirical at the present time.

In these applications the local microstructure or heterogeneity determines the properties of the macromolecular system. In general the experimental measurement of thermodynamic or interfacial properties of these systems is often not practically feasible. Therefore it is not a coincidence that recent journal publications in these areas have focused on newer theoretical and modeling approaches for these systems. Modeling such a system is a multi-scale problem that can be solved for simple fluids given a large parallel computer. For polymeric systems, the problem is more complex for several reasons. First, for polymeric systems, a modest surface–fluid interaction per segment translates to a large surface–fluid interaction per molecule. Second, unlike in simple fluids that are predominantly enthalpy driven, the structure of a complex fluid has a strong entropic driver. Finally, if we consider a polyatomic molecule to be a chain of beads, the range of the heterogeneity is often only over several bead diameters while the size of the polymer may be thousands of bead diameters. In this case a polymeric molecule could exist in the interfacial and bulk regions simultaneously. Therefore, the very notion of "local" molecular density in the inhomogeneous region loses its significance. As bulk polymer theories analyze the system in terms of molecular density, any extension of their arguments to inhomogeneous systems cannot be expected to paint an accurate picture. Traditionally, modeling of polymeric fluids has been motivated by the reasoning that most of the properties of interest depend largely on the long-range structure (Yethiraj, 1996), allowing one to neglect chemical details on short length scales. Recently, it has become increasingly clear that the short-range structure plays an important role in many applications such as coatings of polymer blends (Yethiraj, 1996, 2002). To be able to design and control such applications with confidence, a successful model must incorporate molecular features on all length scales while remaining computationally tractable. Even the most sophisticated existing theories fail to simultaneously meet these criteria (Tripathi, 2005).

To understand the nanoscale features of many polymer-based materials, then, one needs a new class of theoretical methods—something between the traditional atomistic/molecular simulations (length scales of 1–10 Å) and the traditional continuum mechanics or hydrodynamics (length scales usually greater than 100 μm). These new methods—often called mesoscale approaches—cover length scales between 1 and 100 nm and generally deal not with individual atoms (C, H, N, O, etc.) but with "repeat units" or monomers (CH_2, styrene, etc.) as their "building blocks." Tailoring the interactions between these monomers based on the results of atomistic simulations is one way to establish a connection between these two length scales (Baschnagel et al., 2000). For convenience, one often distinguishes between "particle-based" mesoscale simulations (dissipative particle dynamics (DPD), coarse-grained Monte Carlo (CG-MC), and coarse-grained molecular dynamics (CG-MD)) and "field-based" mesoscale theories (density functional theory (DFT) and polymer self-consistent field theory (SCFT)). This chapter mainly deals with the latter methods.

We will highlight the strengths of these theories by focusing on their application to predicting the stability of particles in polymer melts. Nano-size organic or inorganic particles are dispersed in polymer melts to produce polymer nanocomposites. As mentioned, addition of these nanofillers can significantly improve the mechanical, thermal, electrical, and optical properties as compared to the pure polymer or conventional micro- and macrocomposites (Giannelis et al., 1999; Sinha Ray and Okamoto, 2003) without increasing the bulkiness of the host polymer. Polymer/clay nanocomposites are classical examples. Polymer–clay nanocomposites have attained substantial interest in the past two decades, since the successful development of a Nylon-6/montmorillonite hybrid by Okada et al. (1990) at Toyota research laboratories. Since then, hybrid polymer–clay nanocomposites have been successfully prepared using polyethylene (PE), polypropylene (PP), polymethylmethacrylate (PMMA), polystyrene (PS), epoxy, polyurethane, and other matrices (see, e.g., review articles by Sinha Ray and Okamoto 2003 and Alexandre and Dubois 2000). It has been shown that under some conditions, such nanocomposite materials could provide 2–4 times increase in the elastic modulus, order of magnitude decrease in gas permeability, as well as substantial reduction of flammability compared to the pristine polymer matrix, at clay loadings of less than 10 wt.%.

However, one of the challenges in the synthesis of polymer/clay nanocomposites is dispersing the broad clay sheets in the polymer matrix. This depends upon the polymer-mediated interactions between the dispersed particles. The van der Waals and/or electrostatic interactions between the particles are usually attractive, leading to aggregation/flocculation of these particles. Furthermore, it has been shown that for unmodified particles, there is a strong polymer-mediated attraction leading to nanoparticle aggregation (Balazs et al., 1998a, 1999a; Vaia and

Giannelis, 1997a, 1997b); this attraction can be attributed to the fact that polymer chains tend to lose their configurational entropy when confined between colloidal surfaces. The property enhancement, if any, depends strongly on the morphology of the nanocomposite and the quality of nanoclay dispersion in the matrix. In many cases, clay platelets fail to disperse and remain aggregated into large (micron-sized) "stacks" because of polymer-mediated attraction; in this case, modulus and strength of the composite could be comparable to those of the matrix polymer, while toughness and ultimate elongation could even worsen.

One way of stabilizing the dispersion is to end-graft polymers onto the particle surfaces. In that case, positive changes in the configurational entropy of grafted polymer chains (or polymer brushes) can, under certain conditions, counterbalance the negative changes in the configurational entropy of the free polymer (melt) chains and prevent the particles from coming close together. The optimum separation between the grafted particles depends upon the profile of the interaction force. If the force is purely repulsive, the particles are well dispersed into the polymer melt leading to an exfoliated state. In other cases, the force can have an attractive minimum at a finite separation, H^*. Here, the clay sheets will be stacked at separations H^*, leading to an intercalated morphology.

Thus, entropic contributions together with enthalpic factors determine the equilibrium morphology of the polymer/clay nanocomposites. Despite the multidisciplinary interests that surround these systems, many challenges still remain for both experimentalists and theoreticians to understand the interplay of forces and microstructure with the multiple length scales and broad parameter space involved. The interaction between particles in polymer melt, as well as the surrounding fluid structure, is dictated by a number of molecular parameters, including the chain lengths of the grafted and free polymer, grafting density, polymer melt concentration, sizes of the polymer segments, and the nature of the polymer segment–segment interactions. We attempt to investigate the effect of some of these parameters using iSAFT and SCFT, and explore the implications of these effects on modeling of nanocomposite thermodynamics.

2. THEORY

2.1 iSAFT model

Classical DFT is an efficient theoretical tool for prediction of microscopic structure, thermodynamics, and phase behavior of bulk and inhomogeneous fluids, both simple (atomic) and molecular (polymeric) (Evans, 1992; Hansen and McDonald, 1986; Wu, 2006; Wu and Li, 2007). The approach has roots in quantum DFT developed by Hohenberg and Kohn

(1964). Application of DFT as a general methodology to classical systems was introduced by Ebner et al. (1976) in modeling the interfacial properties of a Lennard–Jones (LJ) fluid. The basis of all DFTs is that the Helmholtz free energy of an open system can be expressed as a unique functional of the density distribution of the constituent molecules. The equilibrium density distribution of the molecules is obtained by minimizing the appropriate free energy.

DFTs retain monomer or statistical segment length-level information rather than a more coarse-grained representation of polymers. Thus, DFT provides an approach that is intermediate between macroscopic thermodynamic approaches and truly all atom molecular simulation-based methods. Although the theory incorporates molecular-level detail, calculation time is modest for many systems (Jain et al., 2007). DFT provides a single framework for modeling interfacial, confined, and bulk systems. A thorough review of classical DFT is given by Evans (1992), while many applications of DFT to interfacial systems are described by Davis (1997) and Wu (2006).

Multiple versions of DFT have been developed for polymeric systems (Chandler et al., 1986; Jain et al., 2007; Kierlik and Rosinberg, 1992; Phan et al., 1995; Tripathi and Chapman, 2005a, 2005b; Wu, 2006; Wu and Li, 2007; Yethiraj, 1996, 1998; Yu and Wu, 2002). The theory developed by Chandler, McCoy, and Singer (1986) uses a Taylor series expansion to describe the excess Helmholtz free energy relative to the homogeneous liquid state. The direct correlation function, determined for the homogeneous system using the polymer reference interaction site model (PRISM) (Schweizer and Curro, 1997), is then used to solve for the structure of the inhomogeneous system. This theory has been applied to determine the force between grafted monolayers in an implicit good solvent (McCoy and Curro, 2005).

Owing to the success of Wertheim's thermodynamic perturbation theory (TPT1) (Wertheim, 1984a, 1984b, 1986a, 1986b) for homogeneous systems, several DFTs based on TPT1 have been proposed. The central approximation of any DFT is an expression for the intrinsic Helmholtz free energy of the system. Considering the polyatomic system as a mixture of associating spherical segments in the limit of complete association, the intrinsic Helmholtz free energy functional can be derived from Wertheim's TPT1 as shown in the development of the SAFT equation of state (Chapman, 1988; Chapman et al., 1989, 1990).

In this chapter, we focus on iSAFT, a computationally simple, thermodynamically consistent DFT that accurately predicts the structure and thermodynamics of inhomogeneous polymeric solutions and blends (Jain et al., 2007, 2008, 2009; Tripathi and Chapman, 2005a, 2005b). Like molecular simulation, the DFT uses explicit models of molecules, but the DFT is not limited computationally in molecule size or number of components. The DFT shows excellent agreement with molecular simulation for local structure, compressibility effects, and the effects of molecular size.

In addition to the free polymer and grafted polymer systems shown here, iSAFT has been developed for branched and associating molecules (Bymaster 2010). For a homogeneous fluid, the iSAFT DFT has the advantage that it reduces to an accurate equation of state (SAFT) (Chapman, 1988; Chapman et al., 1989; Jackson et al., 1988; Mueller and Gubbins, 2001), which is widely applied in academia and industry.

In the iSAFT approach, polyatomic molecules are modeled as flexible chains of tangentially bonded spherical segments. Each of the segments of the chains can be different. For simplicity, we present the derivation for a pure fluid of chain molecules with m segments, but the theory is in general applicable to mixtures. Additionally, we will only focus on the physical basis of the derivation leaving out the mathematical details. The details of the derivation can be found in one of the original iSAFT papers (Jain et al., 2007). Additionally, the details of the derivation for extending the theory to grafted polymer chains can be found in Jain et al. (2008, 2009).

DFTs are commonly formulated for an open system in the grand canonical ensemble. Hence, the system is at fixed volume (V), temperature (T), and chemical potential (μ) in the presence of an external field ($V^{ext}(\mathbf{R})$). The appropriate free energy for the grand canonical ensemble is the grand free energy (Ω). The grand free energy functional for a system of chain fluid can be related to the intrinsic Helmholtz free energy functional (A) as

$$\Omega[\rho_\alpha(\mathbf{r})] = A[\rho_\alpha(\mathbf{r})] - \sum_{\alpha=1}^{m} \int d\mathbf{r}' \rho_\alpha(\mathbf{r}') \left(\mu_\alpha - V_\alpha^{ext}(\mathbf{r}')\right), \tag{1}$$

where ρ_α is the density of segment α, μ_α is its chemical potential, and the sum is over all the m segments of the chain. For the system at equilibrium, the grand free energy has to be minimum. Minimization of the grand free energy with respect to density of the segments yields a system of variational equations, known as the Euler–Lagrange equations,

$$\frac{\delta A[\rho_\alpha(\mathbf{r})]}{\delta \rho_\alpha(\mathbf{r})} = \mu_\alpha - V_\alpha^{ext}(\mathbf{r}) \quad \forall \alpha = 1,\ldots,m. \tag{2}$$

Solution of the set of these equations gives the equilibrium density profile of all the segments in the polymer chain. Hence, the central aim of all DFTs is to come up with a formulation of the Helmholtz free energy functional. In iSAFT, we follow an approach similar to that used to develop the SAFT (Chapman et al., 1989, 1990) model for bulk polymer systems, wherein the polymer chains are considered to be a stoichiometric mixture of m associating spherical segments in the limit of complete association, as shown in Figure 1. Following SAFT, we can now write down the free energy functional of this mixture of associating spheres as a perturbation expansion about the free energy of the purely repulsive spheres except that the

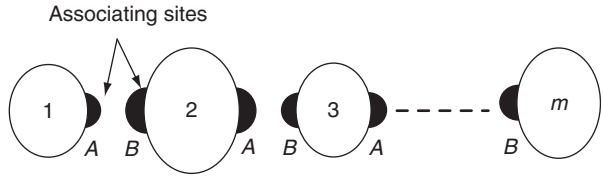

Figure 1 Schematic of the formation of a linear polymer chain of *m* segments from *m* associating spheres. For the middle segment α, site *A* associates with the site *B* on the segment "$\alpha+1$" and site *B* associates with site *A* on the segment "$\alpha+1$." End segments 1 and *m* have only one associating site, *A* or *B*.

various free energies are actually functionals of the segment density profiles. Hence,

$$A[\rho_\alpha] = A^{id}[\rho_\alpha] + A^{EX,hs}[\rho_\alpha] + A^{EX,chain}[\rho_\alpha] + A^{ATT}[\rho_\alpha], \tag{3}$$

where ideal free energy functional *id* plus *EX, hs* accounts for the excluded volume of the segments, and *EX, chain* for the chain connectivity. These three terms together account for the entropic interactions and *ATT* adds on the attractive interactions between the segments of the polymeric fluid mixture.

The ideal gas free energy functional is defined exactly from statistical mechanics, dropping the temperature-dependent terms that do not affect the fluid structure. Free energy functional contribution due to the excluded volume of the segments is calculated from Rosenfeld's (1989) DFT for a mixture of hard spheres. The functional derivatives of these free energy functional contributions, which are actually required to solve the set of Euler–Lagrange equations, are straightforward.

The free energy functional contribution due to chain connectivity lies at the heart of the iSAFT. We start with the free energy functional of a mixture of associating spheres with finite association between them following the extension of the Wertheim's first-order thermodynamic perturbation theory (TPT1) (Wertheim, 1984a, 1984b, 1986a, 1986b) to mixtures of associating spheres (Chapman et al., 1986; Joslin et al., 1987; Segura et al., 1997; Tripathi and Chapman, 2005a, 2005b) and take the limit of complete association between them at a convenient point in the derivation.

For finite association

$$\beta A^{EX,assoc}[\rho_\alpha] = \int d\mathbf{r}_1 \sum_{\alpha=1}^{m} \rho_\alpha^{seg}(\mathbf{r}_1) \sum_{A\in\Gamma^{(\alpha)}} \left(\ln X_A^\alpha(\mathbf{r}_1) - \frac{X_A^\alpha(\mathbf{r}_1)}{2} + \frac{1}{2} \right), \tag{4}$$

where the first summation is over all the segments α, and second over all the association sites on segment α, as $\Gamma^{\{\alpha\}}$ is the set of all the associating

sites on segment α. X_A^α denotes the fraction of segments α that are not associated at their site A. X_A^α depends upon $X_B{}^{\alpha'}$ by

$$X_A^\alpha(\mathbf{r}_1) = \frac{1}{1 + \int d\mathbf{r}_2 X_B^{\alpha'}(\mathbf{r}_2)\Delta^{\alpha\alpha'}(\mathbf{r}_1, \mathbf{r}_2)\rho_{\alpha'}^{seg}(\mathbf{r}_2)}, \tag{5}$$

where α' denotes the segment with site B which associates with site A on segment α, and Δ accounts for the strength of association between these neighboring segments α and α'. In limit of complete association, $X_A^\alpha \to 0$. The limit is taken while computing the functional derivate of the association free energy functional which is required to solve the set of Euler–Lagrange equations. This functional derivative was derived in the original iSAFT paper (Jain et al., 2007):

$$\frac{\delta\beta A^{EX,chain}}{\delta\rho_\alpha(\mathbf{r})} = \sum_{A\in\Gamma^{(\alpha)}} \ln X_A^\alpha(\mathbf{r}) - \frac{1}{2}\sum_{\gamma=1}^{m}\sum_{\gamma'}^{\{\gamma'\}}\int \rho_\gamma(\mathbf{r}_1)\frac{\delta \ln \quad y_{contact}^{\gamma\gamma'}\left[\{\overline{\rho}_\alpha(\mathbf{r}_1)\}\right]}{\delta\rho_\alpha(\mathbf{r}_1)} d\mathbf{r}_1, \tag{6}$$

where $\{\gamma'\}$ is the set of all segments bonded to segment γ, $y^{\gamma\gamma'}{}_{contact}$ is the cavity correlation function at the point of contact of segments γ and γ', and it is evaluated for the weighted density of segments $\{\alpha\}$ at position $\mathbf{r}_1$.

The long-range attractive interactions between the segments are included using the mean field approximation, ignoring the pair correlation between the segments:

$$A^{ATT}[\rho_\alpha] = \frac{1}{2}\sum_{\alpha=1}^{m}\sum_{\beta=1}^{m}\int_{|\mathbf{r}_2-\mathbf{r}_1|>\sigma_{\alpha\beta}} d\mathbf{r}_1 d\mathbf{r}_2 u_{\alpha\beta}^{ATT}(|\mathbf{r}_2-\mathbf{r}_1|)\rho_\alpha^{seg}(\mathbf{r}_1)\rho_\beta^{seg}(\mathbf{r}_2), \tag{7}$$

where u^{ATT} is the attraction potential between the segments.

After substituting these functional derivatives, the set of the nonlinear Euler–Lagrange equations is solved for the density profile of the segments. For a linear chain, the density profile of a segment α is (Jain et al., 2007)

$$\rho_\alpha(\mathbf{r}_\alpha) = \exp(\beta\mu_M)\int d\mathbf{r}_1 \ldots d\mathbf{r}_{\alpha-1} d\mathbf{r}_{\alpha+1} \ldots d\mathbf{r}_m \exp\left(\sum_{i=1}^{m}[D'_i(\mathbf{r}_i)]\right)\prod_{i=1}^{m-1}\Delta^{(i,i+1)}(\mathbf{r}_i, \mathbf{r}_{i+1}), \tag{8}$$

where μ_M is the bulk chemical potential of the polymer chains, and $D'_\alpha(\mathbf{r})$ is given by

$$\begin{aligned} D'_\alpha(\mathbf{r}) = {} & \frac{1}{2}\sum_{\gamma=1}^{m}\sum_{\gamma'}^{\{\gamma'\}}\rho_\gamma(\mathbf{r}_1)\frac{\delta \ln y_{contact}^{\gamma\gamma'}\left[\{\overline{\rho}_\alpha(\mathbf{r}_1)\}\right]}{\delta\rho_\alpha(\mathbf{r})} d\mathbf{r}_1 \\ & - \frac{\delta\beta A^{EX,hs}[\rho_\alpha]}{\delta\rho_\alpha(\mathbf{r})} - \frac{\delta\beta A^{ATT}[\rho_\alpha]}{\delta\rho_\alpha(\mathbf{r})} - \beta V_\alpha^{ext}(\mathbf{r}) \end{aligned} \tag{9}$$

As can be seen from the density profiles, there are two important features of iSAFT, which makes it applicable to a range of heterogeneous polymer systems. One is that iSAFT satisfies overall stoichiometry, which means that the average densities of all segments on a molecule in the system are equal. This constraint comes naturally during the derivation of the theory. The second feature is that each segment on the polymer chain knows about the other segments on the chain.

Finally, the equilibrium grand free energy of the fluid mixture is given by

$$\beta\Omega[\{\rho_\alpha(\mathbf{r})\}] = \sum_{i=1}^{m}\int d\mathbf{r}\rho_\alpha(\mathbf{r})\left[D'_\alpha(\mathbf{r}) + V_\alpha^{ext}(\mathbf{r}) + \frac{n\left(\Gamma^{(\alpha)}\right)}{2} - 1\right] + \beta A^{EX,hs} + \beta A^{ATT}. \tag{10}$$

2.2 Extension of iSAFT model to grafted polymer chains

In the case of grafted polymer chains, one of the chain end segments is physically/chemically tethered to a surface. To extend the iSAFT model to such a case, this restraint is incorporated as an external field on the tethered segment of the polymer chains with the boundary condition being the number of chains grafted to the surface (grafting density, ρ_g). The surface is considered to be a flat hard wall and the chains are uniformly distributed over the area of the surface. Hence, this reduces to a one-dimensional (1D) problem, with the relevant dimension along the normal to the wall. The external field exerted by the wall on the tethered segment "1" is

$$V_1^{ext}(z) = \begin{cases} v & \text{if } z = 0 \\ \infty & \text{otherwise} \end{cases} \tag{11}$$

For other segments, the external potential is just due to a planar hard wall. Furthermore,

$$\int dz_\alpha \rho\rho_\alpha(z_\alpha) = \rho_g. \tag{12}$$

Following these arguments, the density profile of segment α ($\alpha \neq 1$) in the grafted polymer chains is

$$\rho_\alpha(z_\alpha) = \rho_g \frac{\int\int dz_2 \ldots dz_{\alpha-1} dz_{\alpha+1} \ldots dz_m \exp\left(\sum_{i=2}^{m}[D'_i(z_i)]\right)\Delta^{(1,2)}(0,z_2)\prod_{i=2}^{m-1}\Delta^{(i,i+1)}(z_i,z_{i+1})}{\int\int dz_2 \ldots dz_m \exp\left(\sum_{i=2}^{m}[D'_i(z_i)]\right)\Delta^{(1,2)}(0,z_2)\prod_{i=2}^{m-1}\Delta^{(i,i+1)}(z_i,z_{i+1})} \tag{13}$$

Clearly, this derivation is only for the polymer chains grafted to the wall at $z=0$. For the case of two grafted surfaces, similar results can be obtained for the polymer chains grafted to the wall at $z=H$, where H is the separation between the two surfaces.

The force of interaction between the two grafted surfaces (in the absence/presence of free polymer) at separation H is given by

$$\frac{f(H)}{A} = \left(-\frac{1}{A}\frac{\delta\Omega}{\delta H}\right)_{H} - \left(-\frac{1}{A}\frac{\delta\Omega}{\delta H}\right)_{H\to\infty}, \tag{14}$$

where Ω is the equilibrium grand free energy, A is the surface area of the two surfaces, and $H\to\infty$ implies the limit when the separation between the two surfaces is large enough that they do not interact with each other. If f is positive, the surfaces repel each other, and if f is negative, they attract. In the current work, the two hard surfaces are grafted with the same polymer chains at the same grafting density. Hence, the density profiles of the two grafted monolayers are symmetric. For such a symmetric system, the functional derivative of the grand free energy can be simplified as (Evans and Marconi, 1987)

$$\frac{1}{A}\frac{\delta\Omega}{\delta H} = \sum_{\alpha}\int \rho_{\alpha}(z)\frac{\mathrm{d}V_{\alpha}^{ext,s}(z)}{\mathrm{d}z}\mathrm{d}z, \tag{15}$$

where $V_{\alpha}^{ext,s}$ is the external field on segment α due to a single surface at $z=0$. For hard walls, this reduces to the sum of the contact densities of the grafted and free polymer chains at the surface at $z=0$. Hence, the structures of the grafted polymer chains (and the free polymer) have to be calculated first before calculating the force of interaction between them.

2.3 Self-consistent field theory

SCFT today is one of the most commonly used tools in polymer science. SCFT is based on de Gennes–Edwards description of a polymer molecule as a flexible Gaussian chain combined with the Flory–Huggins "local" treatment of intermolecular interactions. Applications of SCFT include thermodynamics of block copolymers (Bates and Fredrickson, 1999; Matsen and Bates, 1996), adsorption of polymer chains on solid surfaces (Scheutjens and Fleer, 1979, 1980), and calculation of interfacial tension in binary polymer blends compatibilized by block copolymers (Lyatskaya et al., 1996), among others.

Over the past decade, SCFT was often applied to analyze the problem of particle dispersion in polymers (thermodynamics of nanocomposites). Vaia and Giannelis (1997a, 1997b) formulated a simple version of SCFT

that provided qualitative description of exfoliated, intercalated, and immiscible morphologies by estimating the free energy of the polymer and organic modifier confined between two adjacent parallel surfaces separated by a gallery with a width H. Subsequently, Balazs and co-workers (Balazs et al., 1998b, 1999b, 2000, 2008; Ginzburg and Balazs, 2000; Ginzburg et al., 2000; Zhulina et al., 1999) utilized a more elaborate Scheutjens–Fleer version of SCFT to generate various nanocomposite phase diagrams (e.g., how the composite morphology depends on the ratio of the grafted chain length to the matrix chain length) In particular, in a practically important case of organically modified clays in a homopolymer melt, it was shown that clay platelets could favor aggregation even when there is no enthalpic repulsion between the matrix polymer and the surfactant (Flory–Huggins parameter $\chi_{PS} = 0$), provided that the surfactant has low chain length and high grafting density. This prediction was indeed confirmed for cases like the mixtures of montmorillonite clay with C16 or C18 grafted chains, melt-compounded with polyethylene or polypropylene; such systems were demonstrated to be mostly immiscible, in agreement with theoretical predictions (Balazs et al., 2000; Lyatskaya and Balazs, 1998; Sinha Ray and Okamoto, 2003). Similarly, for the cases where end-functionalized chains (e.g., maleated polypropylene) were added to the melt, intercalated and exfoliated morphologies could be observed (Beyer et al., 2002; Hasegawa et al., 2000; Sinha Ray and Okamoto, 2003), as predicted by the theory.

In our view, one area where SCFT predictions are not fully satisfactory is in explaining intercalated morphologies. Indeed, there are numerous nanocomposite systems exhibiting intercalated morphology with a typical gallery spacing $H^* \sim 1$–$2\,\text{nm}$ (10–20 Å). While conventional SCFT does predict intercalated morphologies in various systems (Balazs et al., 1998b, 1999a,), the gallery spacing corresponding to those structures is expected to be somewhat larger than observed (probably on the order of 4–10 nm, depending on the molecular weight of the functionalized chains). Furthermore, in recent experimental studies by Swain and Isayev (2007), intercalated structures have been reported even in systems without "stickers" (Cloisite 20A in high-density polyethylene) when they were subjected to strong ultrasound treatment in the melt state. The increase in the clay–clay spacing (compared to the pure organoclay), measured by wide-angle X-ray scattering (WAXS), was fairly small (from 2.4 to 3.56 nm). In a sense, it appears that intercalated structures are far more ubiquitous than originally predicted by the theory. We proposed (Ginzburg et al., 2009) that the origin for this discrepancy was due to the "incompressible" nature of the SCFT approaches. Accordingly, we formulated a "compressible" extension of the SCFT model for nanocomposites and applied it to the specific case of organoclay mixed with a blend of homopolymer and a "one-sticker" polymer.

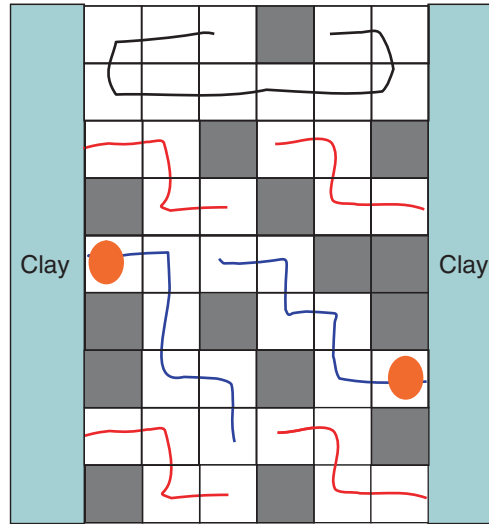

Figure 2 Schematic depiction of the lattice model. Note that some of the lattice sites are not occupied by polymeric species—those are "voids."

Our lattice model is schematically depicted in Figure 2. In its most general form, the grand canonical free energy per unit area, f, is written as

$$f = \frac{G}{Ma^2 k_B T} = \sigma \ln\left(\frac{\sigma N_g}{\sum_{z=1}^{H} G_g(z, N_g)}\right) + \sum_i \frac{\Theta_i}{N_i} \ln \varphi_i^b + \Theta_v \ln \varphi_v^b - \sum_i \mu_i \frac{\Theta_i}{N_i} - \mu_v \Theta_v$$
$$+ {}^1/_2 \left(\sum_{z=1}^{H}\left(\sum_{\alpha,\beta} \chi_{\alpha\beta}\left(\phi_\alpha(z) - \phi_\alpha^b\right)\left(\langle\phi_\beta(z)\rangle - \phi_\beta^b\right)\right)\right) - \sum_{z=1}^{H}\left(\sum_\alpha u_\alpha(z)\phi_\alpha(z)\right) \tag{16}$$

Here, a is the lattice unit dimension, M is the number of lattice units per clay platelet (so that the product $Ma^2 = A$ is the total area of the platelet), σ is the grafting density of "surfactants," $\chi_{\alpha\beta}$ are the Flory–Huggins parameters between species α and β, μ_i is the chemical potential of the ith component, and Θ_i is the excess amount of the ith component in the system. The density profiles of various species, $\phi_\alpha(z)$, and conjugate fields, $u_\alpha(z)$, are calculated as described below. Note that we introduce a separate species and component—voids (denoted as subscript v)—to account for density variation within the gallery.

The bulk chemical potentials of all polymers and voids are described as

$$\mu_i = \ln \varphi_i^b + (1 - N_i)\left(1 - \varphi_i^b\right), \tag{17a}$$

$$\mu_v = \ln \varphi_v^b + \sum_i \frac{\varphi_i^b}{N_i}(1 - N_i). \tag{17b}$$

In Equations (17a) and (17b), densities with superscript b refer to the equilibrium densities in the bulk (for all components and all species). The excess amount of each component, Θ, is given by

$$\Theta_i = \sum_{z=1}^{H} \phi_i(z), \tag{18a}$$

$$\Theta_v = \sum_{z=1}^{H} \phi_v(z). \tag{18b}$$

The effective fields, $u_\alpha(z)$ and $u_v(z)$, are given by

$$u_\alpha(z) = u'(z) + \frac{1}{2}\sum_\beta \chi_{\alpha\beta}\{\langle\phi_\alpha(z)\rangle - \varphi_\alpha^b\}, \tag{19a}$$

$$u_v(z) = u'(z) + \frac{1}{2}\sum_\beta \chi_{\beta v}\left\{\langle\phi_\beta(z)\rangle - \varphi_\beta^b\right\}. \tag{19b}$$

The effective hard core potential $u'(z)$ is a Lagrange multiplier that enforces the incompressibility condition

$$\sum_\alpha \phi_\alpha(z) + \phi_v(z) + \phi_g(z) = 1. \tag{20}$$

To complete the set of equations needed to calculate the free energy and density profiles, one needs the rules to evaluate density profiles. The local density of the voids, $\phi_v(z)$, is calculated always from Equation (20), while the calculation of the density of the polymeric components is more complicated and depends on the specific composition of the bulk polymer and the architecture of each polymeric component. We restrict ourselves to the systems in which the bulk contains two types of polymer: "free" or "matrix" homopolymer chains, and "active" or "end-functionalized" chains with one "sticker." For each type of chain (including the grafted surfactants), one can evaluate the "propagators" $G(z,s)$ and $G^*(z,s)$. (The propagators are evaluated assuming Markov statistical process for Gaussian chains occupying various lattice sites.) All the propagators obey the same recurrence equation

$$Y(z,s) = \langle Y(z,s-1)\rangle G_{t(s)}(z). \tag{21}$$

Here, Y is a shorthand for one of the five propagators: $G_g(z,s)$ and $G_g^*(z,s)$ (for grafted chains), $G_a(z,s)$ and $G_a^*(z,s)$ (for "active" chains), and $G_f(z,s)$ (for "free" chains; because of symmetry, $G_f^*(z,s) = G_f(z,s)$). The factor $G_\alpha(z)$ is

the Boltzmann factor for the species of type α to be at position z compared to the bulk:

$$G_\alpha(z) = \exp(-u_\alpha(z)). \tag{22}$$

In Equation (21), index $t(s)$ labels the species type of a monomer having position s in the chain. For the case of "free" chains, all monomers are the same (we label them as "F"):

$$\phi_F(z) = \sum_{s=1}^{N_f} \left(\frac{\varphi_f^b}{N_f} \right) \frac{G_f(z,s) G_f\left(z, N_f - s + 1\right)}{G_F(z)}. \tag{23a}$$

For the grafted chains, all monomers are also the same (we label them as "G"):

$$\phi_G(z) = \sum_{s=1}^{N_g} \left(\frac{\sigma}{\sum_{z'=1}^{H} G_g\left(z', N_g\right)} \right) \frac{G_g(z,s) G_g^*\left(z, N_g - s + 1\right)}{G_G(z)}. \tag{23b}$$

Finally, for active chains, there are two types of monomers: "sticker" (at position $s = 1$) and the rest (positions $s = 2$ to N_a), labeled as "S" and "A," respectively:

$$\phi_S(z) = \sum_{s=1}^{1} \left(\frac{\varphi_a^b}{N_a} \right) \frac{G_a(z,s) G_a(z, N_a - s + 1)}{G_S(z)}, \tag{23c}$$

$$\phi_A(z) = \sum_{s=2}^{N_a} \left(\frac{\varphi_a^b}{N_a} \right) \frac{G_a(z,s) G_a(z, N_a - s + 1)}{G_A(z)}. \tag{23d}$$

In Equations (16), (19), and (21), $\langle \ldots \rangle$ denotes local averaging according to the prescription

$$\langle Y(z) \rangle = \lambda_{-1} Y(z-1) + \lambda_0 Y(z) + \lambda_1 Y(z+1) \tag{24}$$

Constants λ_{-1}, λ_0, and λ_1 are determined by the choice of the lattice; in our calculations, $\lambda_{-1} = \lambda_1 = 0.25$ and $\lambda_0 = 0.5$. This choice corresponds to the simple cubic lattice, which is commonly used in the application of lattice SCFT to polymer–clay composites. To relate the lattice coordinate to "real" dimensions, we must also specify the value of the lattice size a; here, we set $a = 0.4$ nm. (Later, in Section 3.5, when describing our results, we will automatically convert all distances from lattice units to nanometers.)

Recursive relation (21) must be solved for $s = 1$ to N_f for the free chain propagator $G_f(z,s)$, for $s = 1$ to N_g for the grafted chain related propagators $G_g(z,s)$ and $G_g^*(z,s)$, and for $s = 1$ to N_a for the active chain propagators $G_a(z,s)$ and $G_a^*(z,s)$. The initial conditions are as follows: $G_f(z,1) = G_F(z)$, $G_g(z,1) = G_G(z)\delta_{z1}$, $G_g^*(z,1) = G_G(z)$, $G_a(z,1) = G_S(z)$, and $G_a{}^*(z,1) = G_A(z)$.

Equations (16)–(24) are solved on a lattice in an iterative fashion until a convergence criterion (e.g., the difference between free energy calculations from the two successive iterations) is satisfied.

The free energy profiles *f(H)* and the density profiles of various species and components (including the voids) are used to characterize the nanocomposite morphology and decide whether the system tends to be in exfoliated, intercalated, or immiscible state. Note that because of the "compressibility" (non-zero bulk volume fraction of voids), SCFT results could be compared to iSAFT results. We will attempt such a comparison in Section 3.2 for the "athermal" (all Flory–Huggins $\chi_{\alpha\beta}=0$) case with no active chains. Additionally, in Section 3.4, we explore SCFT phase diagram for a system in which active "one-sticker" chains are present and compare our predictions with the earlier results of Ginzburg and Balazs that were based on the "incompressible" SCFT; it will be shown that the new approach dramatically expands the region corresponding to intercalated morphologies.

3. APPLICATIONS

This section highlights the applications of iSAFT and SCFT to predict the stability of grafted particles dispersed in a polymer solution. We consider cases where the surfaces of the grafting particles are significantly larger than the height of the monolayers formed by the polymer chains grafted onto those particles. In this limit, the grafted surfaces can be treated as planar. The stability of these particles depends upon the effective force of interaction between such grafted (planar) surfaces. For example, one of the challenges in the synthesis of polymer/clay nanocomposites is dispersing the broad clay sheets in the polymer matrix. This depends upon the polymer-mediated interactions between the dispersed particles. The van der Waals and/or electrostatic interactions between the particles are usually attractive leading to aggregation/flocculation of these particles and worsening the properties of the nanocomposite. This attraction can be attributed to the fact that polymer chains tend to lose their configurational entropy when confined between colloidal surfaces. One way of stabilizing the dispersion is to end-graft polymers onto the particle surfaces. In that case, positive changes in configurational entropy of grafted polymer chains can, under certain conditions, counterbalance the negative changes in the configurational entropy of the free polymer (melt) chains. Thus, the effective interactions between the grafted surfaces determine the stability of the nanocomposite.

We will begin with the structure of unperturbed polymer monolayers in the presence of a solvent and then move on to the case of two polymer grafted surfaces in the presence of a polymeric fluid, discussing

the structure of the grafted monolayers and the effective force of interaction between the grafted surfaces. Wherever possible, we have directly compared iSAFT and SCFT predictions.

3.1 Structure of grafted polymer monolayers in the presence of a polymer melt

Molecular dynamics simulations for grafted polymer monolayers in the presence of free polymer melt have been done by Grest and Murat (1993). The calculations are done for free polymer chains with few segments ($N_f = 2$, 5, and 10). Both the grafted and the free polymer chains are purely repulsive and have the same segment sizes ($\sigma_g = \sigma_f = \sigma$), where σ_g and σ_f are the segment sizes of the grafted and free polymer chains, respectively. The overall density of the segments in the system is quite large, $\rho_{tot}\sigma^3 = 0.85$. The number of segments in the grafted chains is fixed to $N_g = 100$ and the grafting density is fixed to $\rho_g\sigma^2 = 0.1$. The density of free polymer for all the three cases, $N_f = 2$, 5, and 10, is $\rho_f\sigma^3 = 0.682$, based on the overall segment density in the system. Figure 3a compares the density profiles of the monolayers for these three cases with that in the presence of an implicit solvent ($N_f = 0$). As can be seen from the figure, the presence of an explicit solvent (free polymer) significantly affects the structure of the monolayers. Since the chains are purely repulsive, the origin of the effect is solely due to the entropic interactions. Due to volume exclusion, the explicit solvent molecules compress the grafted polymer chains causing them to partially collapse compared to the case

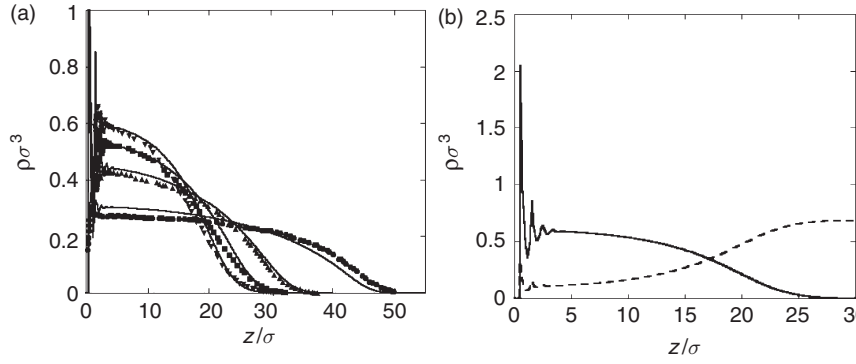

Figure 3 (a) Segment density profiles of grafted chains, $N_g = 100$ and $\rho_g\sigma_g^2 = 0.1$, in the presence of implicit solvent (●) and explicit free chains with $N_f = 2$ (▲), $N_f = 5$ (■), and $N_f = 10$ (▼). Symbols are the simulation results from Grest and Murat (1993) and curves are the predictions from iSAFT. (b) Solid line represents segment density profiles of grafted polymer chains ($N_g = 100$ and $\rho_g\sigma_g^2 = 0.1$) and Dashed line represents density profiles of the free polymer solvent ($N_f = 10$ and $\rho_f\sigma_f^3 = 0.682$) from iSAFT.

of implicit solvent. This compression increases with the increase in the number of segments in the solvent polymer chains and the height of the monolayers decreases further. As the solvent density is large, the solvent chains penetrate into the monolayer, as seen in Figure 3b. However, near the wall, the segments of the grafted polymer chains dominate where there is a strong layering because of the presence of the hard surface.

3.2 Interaction between two grafted monolayers in the presence of free polymer melt with both the grafted and the free polymer chains having equal segment sizes

Now, we consider two grafted surfaces. Both the grafted and the free polymer chains are purely repulsive and have the same segment sizes ($\sigma_g = \sigma_f = \sigma$). For large separations between them, they do not interact and behave as two independent monolayers immersed in the free polymer melt. These monolayers and the free polymer interpenetrate each other and the monolayers are compressed. The degree of interpenetration depends upon the chain lengths of the grafted (N_g) and free (N_f) polymers, grafting density ρ_g, and the bulk free polymer density ρ_f. As all the polymer chains are purely repulsive, they are implicitly in good solvent condition. Figure 4a shows the segment density profiles of the grafted and free polymers for $N_g = 101$, $\rho_g\sigma^2 = 0.1$, $N_f = 100$, and $\rho_f\sigma^3 = 0.2$, when the grafted monolayers are far apart. Each monolayer interpenetrates the free polymer to a certain extent after which the free polymer reaches its bulk density. The monolayers start interacting as the separation is reduced. In addition to penetrating the free polymer, the monolayers themselves interpenetrate each other. In doing so, they expel the free polymer between them and the density of the free polymer decreases, as shown in Figures 4b and 4c. Eventually, at low enough separation, almost all the free polymer leaves the gap between the monolayers, as shown in Figure 4d.

Let us now turn to the discussion of the SCFT results and compare them with the iSAFT calculations. In our calculations, we use the following parameters: $N_f = 100$, $N_g = 100$, $\rho_g{}^* = 0.1$. The statistical segment length a in SCFT calculations and the segment size σ in iSAFT calculations are assumed to be equal and the volume fraction of the free polymer in the bulk, φ_f^b, in SCFT calculations equal to the free polymer density, $\rho_f\sigma^3$, in iSAFT calculations, so that we can attempt exact comparison with the iSAFT analysis. Density profiles and grand canonical free energy, $F(H)$, are evaluated as function of the separation between the plates, H (expressed in units of a). Taking a derivative of F with respect to H, one can calculate the normal force of interaction between the grafted monolayers and compare it with the one estimated using iSAFT. For calculations, we utilized the code Polymer developed by P. Linse (Lund University).

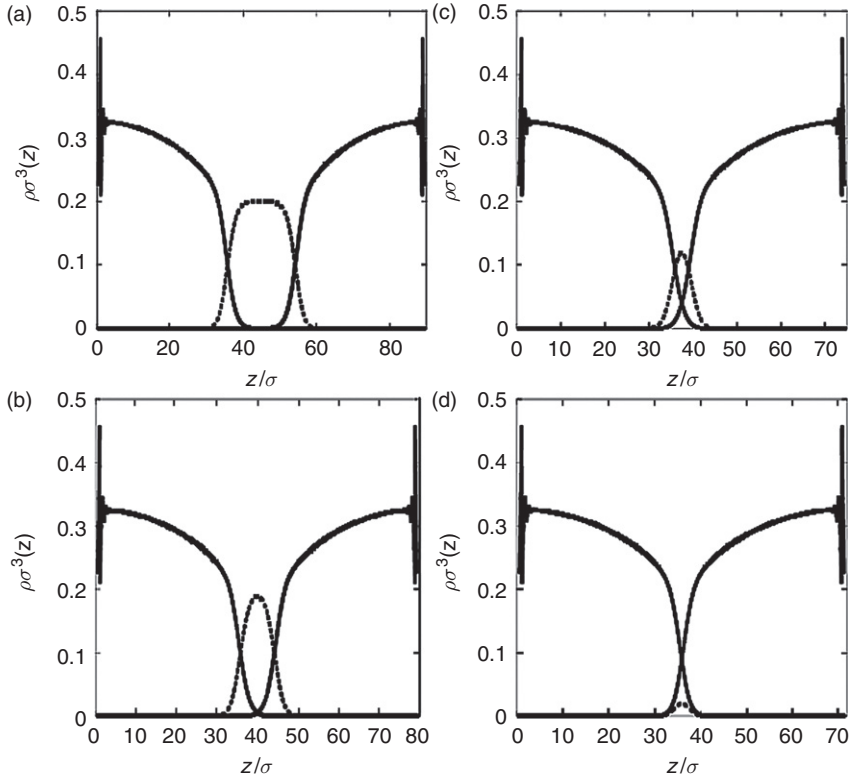

Figure 4 Segment density profiles of the two grafted monolayers (solid curves) and the free polymer (dotted curves) at separations (a) $H = 90\,\sigma$, (b) $H = 80\,\sigma$, (c) $H = 75\,\sigma$, and (d) $H = 72\,\sigma$. Parameters: $N_g = 101$, $\rho_g\sigma_g^2 = 0.1$, $N_f = 100$, $\rho_f\sigma_f^3 = 0.1$, and $\sigma_g = \sigma_f = \sigma$.

In Figure 5a, we plot the density profiles for the free polymer and grafted polymer for $H = 50$, with bulk polymer volume fraction set to 0.75. The agreement between the densities predicted by the two methods is surprisingly good. The main difference is in the behavior near the hard surfaces. While SCFT predicts pronounced polymer depletion near the walls, iSAFT calculations show strong, almost diverging, density fluctuations near the surfaces. In the bulk, the predictions of the two theories agree not just qualitatively, but even semi-quantitatively. In Figure 5b, we plot the density profiles for the system with bulk polymer volume fraction of 0.25 and $H = 80$. Here, the agreement between the two theories is much worse. SCFT appears to over-predict the amount of free polymer drawn into the gallery (compared to iSAFT); it also predicts more diffuse distribution of the free polymer and the grafted (brush) polymer, as compared to iSAFT.

In Figure 6, we plot the effective force of interaction between the monolayers from iSAFT and SCFT as a function of the distance H between

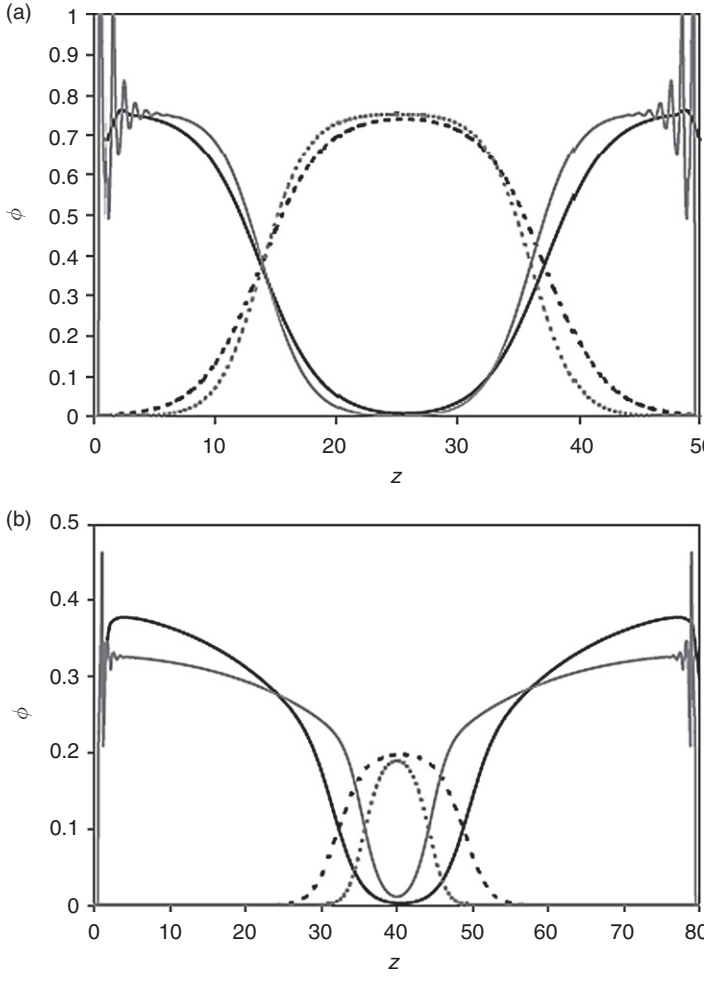

Figure 5 Density profiles of grafted (solid curves) and free polymer chains (dotted curves) as a function of the spatial coordinate z, calculated using iSAFT (gray curves) and SCFT (black curves) methods. (a) Free polymer bulk volume fraction $\varphi_f^b = 0.75$; separation between the platelets $H = 50$, and (b) free polymer bulk volume fraction $\varphi_f^b = 0.2$; separation between the platelets $H = 80$. Other parameters: $N_g = 101$, $\rho_g^* = 0.1$, and $N_f = 100$.

them. It is instructive to consider the differences between the curves corresponding to various free polymer volume fractions.

iSAFT and SCFT curves for the highest bulk polymer volume fraction ($\varphi_f^b = 0.75$) lie very close to each other. For that system, both models predict, effectively, purely repulsive behavior: when the two monolayers are far apart, normal force is practically zero; when the monolayers are

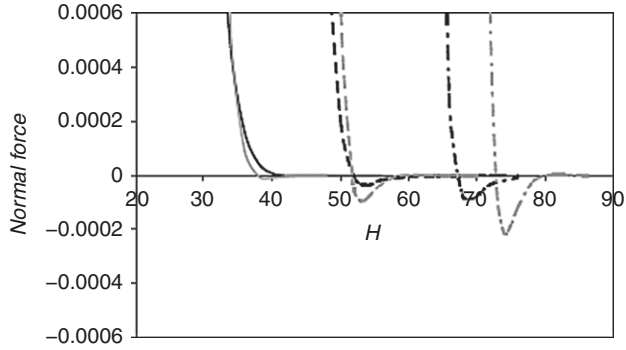

Figure 6 Normal force per unit area between the plates as a function of their separation, calculated using iSAFT (gray curves) and SCFT (black curves). Free polymer bulk volume fractions: 0.2 (dotted-dashed curves), 0.4 (dashed curves), and 0.75 (solid curves). Other parameters: $N_g = 101$, $\rho_g^* = 0.1$, and $N_f = 100$.

beginning to interact ($H < 40$), repulsive force appears and rapidly grows as H is decreased. For the intermediate polymer volume fraction ($\varphi_f^b = 0.4$), there is effective repulsion at small distances ($H < H^*$) and attraction at large distances ($H > H^*$). The critical separation, H^*, is approximately equal to 50 (from both iSAFT and SCFT). We note that the attractive force predicted by iSAFT is stronger than that predicted by SCFT; however, the inherent error in determining the normal force in SCFT is relatively high because of the need for numerical calculation of the free energy derivative. Finally, for the smallest free polymer bulk volume fraction ($\varphi_f^b = 0.2$), there is some discrepancy in the prediction of H^* (68 from SCFT, 72 from iSAFT); the attractive force estimated by iSAFT is once again stronger than that predicted by SCFT.

Altogether, considering the differences between the two methods, the results appear to be in a remarkably good agreement. It is interesting that the best agreement—qualitative and quantitative—between the two methods corresponds to the high polymer volume fraction conditions ($\varphi_f^b = 0.75$). It is well documented that the accuracy of SCFT is the highest for the "incompressible melt" conditions ($\varphi_f^b \to 1$) and decreases as the fraction of "voids" goes up; on the other hand, iSAFT is expected to work best at low to intermediate polymer concentrations but fail when φ_f^b becomes too high. Our analysis shows that—at least for the athermal systems considered here—one could accomplish a smooth, continuous transition from iSAFT description (low polymer concentration) to SCFT description (high polymer concentration). Whether this continuous transition could be accomplished in other (especially non-athermal) systems will be the subject of future studies.

The results depicted in Figure 6 have interesting implications for nanocomposite thermodynamics. If the "density" (bulk polymer volume

fraction) is sufficiently high, the equilibrium nanocomposite morphology is expected to be exfoliated (normal force between the platelets is always repulsive). However, at intermediate to low bulk polymer volume fractions, a pronounced attractive force region appears, indicating preference for intercalated morphology. This is due to the fact that voids could easily enter the "gallery" between the two surfaces, while the "free" polymer is pushed out of the gallery where its entropy is lower than in the bulk. Thus, let us consider the changes in the gallery as we reduce its width, H. At first, free polymer is squeezed out; the intra-gallery space is enriched by voids, free energy decreases, and normal force is attractive. However, as the two brushes come closer, the system can no longer expel the free polymer because of the growing imbalance between the intra-gallery and bulk compositions; at that point, the free energy would begin to increase, and normal force would change sign from attractive to repulsive. Thus, including melt compressibility in the analysis of nanocomposite thermodynamics provides a potential new mechanism favoring intercalated morphologies over exfoliated ones.

Similar behavior for the interaction force is observed on changing the chain length of the free polymer while keeping its bulk density fixed, as shown in Figure 7. The interaction force is purely repulsive for the smallest free polymer chain length, while at larger chain lengths, the force is attractive at intermediate separations and repulsive at lower separations. There is a higher entropic advantage for the free ends of the two monolayers to mutually overlap each other rather than the two monolayers overlapping with the longer free polymer chains. Hence, the attractive region increases with the increase in the free polymer chain length.

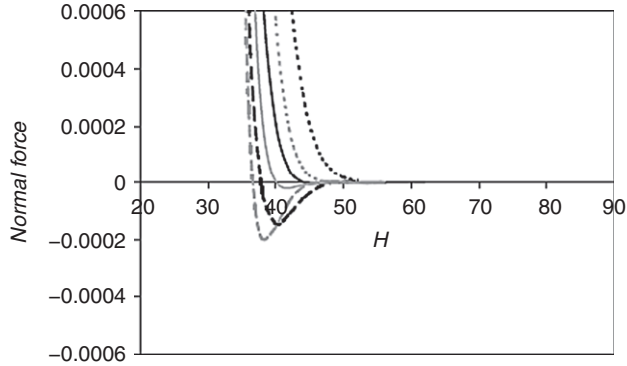

Figure 7 Normal force per unit area between the plates as a function of their separation, calculated using iSAFT (gray curves) and SCFT (black curves). Free polymer chain lengths: 50 (dotted curves), 100 (solid curves), and 150 (dashed curves). Other parameters: $N_g = 101$, $\rho_g^* = 0.1$, and $\varphi_f^b = 0.6$.

Furthermore, the attractive region occurs only when the free polymer exceeds a certain minimum chain length. If the free polymer chain length is lower than this value, then the force is purely repulsive. For $N_g = 101$, $\rho_g\sigma^2 = 0.1$, and $\rho_f\sigma^3 = 0.6$, this critical value of N_f lies somewhere between 50 and 100, as shown in Figure 7.

Again, the agreement between iSAFT and SCFT is remarkable. The agreement is best (qualitatively as well as quantitatively) at the highest free polymer chain length, $N_f = 150$. For both $N_f = 150$ and 100, the attractive regions predicted by iSAFT are stronger than that predicted by SCFT. In fact, for $N_f = 100$, the attractive region predicted from SCFT is so small that it can be hardly be seen in the figure. Hence, the critical value of N_f, at which the force of interaction between the grafted monolayers turned from purely repulsive to having an attractive minimum, calculated using SCFT lies closer to 100 than that from iSAFT. However, this value still lies between 50 and 100.

Using iSAFT, we further calculated the critical chain lengths of the free polymer for a number of cases at different bulk free polymer densities, grafting densities, and chain lengths of the grafted polymer. We found that it is the ratio of the chain lengths of the free and grafted polymers, $\alpha = N_f/N_g$, that determines whether the force of interaction between the monolayers is purely repulsive or has an attractive minimum. Figure 8 plots the loci of the critical values of α at which the force of interaction between the grafted monolayers turned from purely repulsive to having

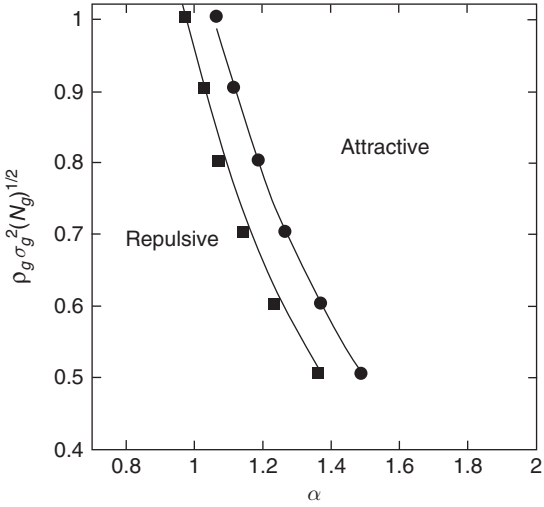

Figure 8 Locus of the critical values of α at which the interaction between the grafted monolayers becomes attractive for different bulk free polymer densities: $\rho_f\sigma_f^3 = 0.6$ (■) and $\rho_f\sigma_f^3 = 0.75$ (●). $N_g = 101$ and $\sigma_g = \sigma_f = \sigma$.

an attractive minimum, for different bulk free polymer densities. The locus (at a fixed free polymer density) calculated using iSAFT agrees with the scaling relation obtained from previous theoretical studies using Strong Segregation Theory (SST) (Leibler et al., 1994) and numerical SCFT (Ferreira et al., 1998; Matsen and Gardiner, 2001): $\rho_g\sqrt{N_g} \propto \alpha^{-\lambda}$, where λ is the scaling exponent. From iSAFT, $\lambda = 2$.

3.3 Interaction between two grafted monolayers in the presence of free polymer melt with the grafted and free polymer chains having different segment sizes

Next, we consider the case where the segment sizes of the polymer in the monolayers and the free polymer are not identical, which is not easily accessible to SCFT. To our knowledge, other theoretical models have not previously addressed this case as well. Using iSAFT, we investigate the effect of changing the relative sizes of the segments in the free and grafted polymers, $\beta = \sigma_f/\sigma_g$, on the interaction force between the grafted monolayers. We found that even for $\sigma_f \neq \sigma_g$, the repulsion/attraction boundaries follow the same scaling relation, $\rho_g\sqrt{N_g} \propto \alpha^{-\lambda}$ (at fixed free polymer density). The boundaries shift toward the attractive domain as β decreases, or, in other words, the critical value of α increases as the relative segment size of the grafted polymers increases. This is due to the fact that the steric hindrance is higher for grafted monolayers with bigger segments. The steric hindrance between the two monolayers depends upon the volume of the segments of grafted polymers; hence, intuitively, different repulsion/attraction boundaries for different segment sizes of the grafted polymer (relative to the size of free polymer segments) may scale by ${\sigma_g}^3$. In fact, this is the case as shown in Figure 9. The figure shows that for cases where the relative segment sizes of the grafted and free polymers are different, the critical value of α where the interaction force between the two monolayers turns from purely repulsive to attractive follows the scaling relation, $\rho_g\sqrt{N_g}\beta^3 \propto \alpha^{-2}$.

3.4 Interaction between two grafted monolayers in the presence of attractive chains

Now we consider the attraction between the segments of the tethered and the free polymer chains. To make it realistic, the attractive LJ energy is based on that of polypropylene segments. The energy parameter $\varepsilon/k = 235$ K is calculated from the correlation given by Dominik et al. (2006) using its value from perturbed-chain (PC)-SAFT (Gross and Sadowski, 2002, 2003; Tumakaka et al., 2002) (PC-SAFT $\varepsilon/k = 217$ K). For the polypropylene melt at $T = 170$°C, the dimensionless parameters are

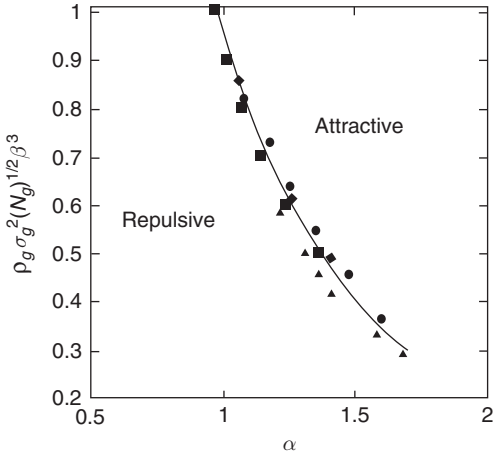

Figure 9 Scaling relation for the locus of the critical values of α at which the interaction between the grafted monolayers becomes attractive for different relative segment sizes of the grafted and free polymer: $N_g = 101$ and $\sigma_g = \sigma_f$ (■), $N_g = 101$ and $\sigma_g = 1.1\,\sigma_f$ (●), $N_g = 101$ and $\sigma_g = 1.2\,\sigma_f$ (▲), and $N_g = 151$ and $\sigma_g = \sigma_f$ (◆). The bulk free polymer density $\rho_f \sigma_f^3 = 0.6$. $\sigma_f = \sigma$.

$\rho_f \sigma^3 = 0.75$ and $\varepsilon/kT = 0.53$. This energy parameter was used for both tethered chains and free chains.

The values of α_c for this system as a function of the grafting density ρ_g are calculated using a sort of bisection scheme. At a fixedρ_g, the forces of interaction are calculated as a function of the separation for two extreme values of α, such that the lower value α_1 shows pure repulsion and the higher value α_2 shows the attractive minimum in the force curve. $\{\alpha_1,\alpha_2\}$ is the initial set such that α_c lies between α_1 and α_2. Then the force curve is calculated at the midpoint, $(\alpha_1 + \alpha_2)/2$. If the force is purely repulsive at this value of α, then $\{(\alpha_1 + \alpha_2)/2,\alpha_2\}$ is the new set otherwise $\{\alpha_1,(\alpha_1 + \alpha_2)/2\}$ forms the new set. These steps are repeated till $\alpha_{att} - \alpha_{rep} = 0.5$, such that the force is purely repulsive for α_{rep} and shows a minimum forα_{att}. Figure 10 shows these values of α_{rep} and α_{att} for different values of ρ_g. There are two reasons for reporting this band which contains α_c rather than exactly pinpointing the value of α_c. Although there is a minimum for values of α greater than α_c, for values of α closer to α_c the minimum is so shallow that it is difficult to ascertain it numerically. However, for $\alpha \geq \alpha_{att}$, the attractive minimum is significant.

To sum up the result shown in Figure 10, the dispersion is stable if the value of α lies on the left side of solid curve in the figure and it is unstable (causes agglomeration) if the value of α lies on the right side of the dashed curve. Hence, the values of α on the dashed curve give the optimum chain length of the tethered chain to create a stable dispersion.

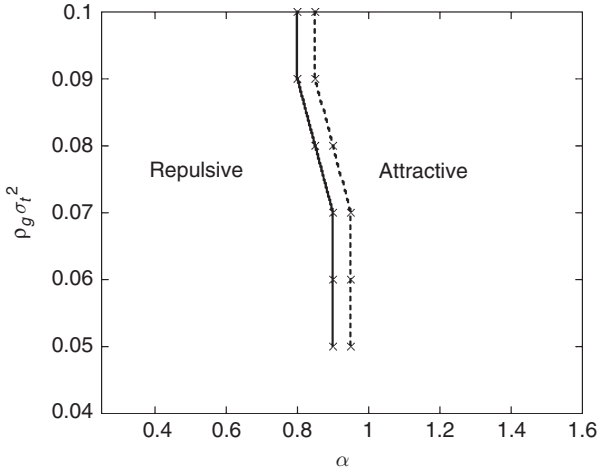

Figure 10 Stable (repulsive) versus unstable (attractive) dispersion of tethered chains as a function of the ratio of the polymer chain length to tethered polymer chain length (α).

3.5 Interaction between two grafted monolayers in the presence of end-functionalized chains

Here, again, we start from compressible SCFT formalism described in Section 2.2 and consider a model system in which bulk polymer consists of "free" matrix chains ($N_f = 300$) and "active" one-sticker chains ($N_a = 100$). Flory–Huggins interaction parameters between various species are summarized in Table 1. This corresponds to the scenario in which surfactants, matrix chains, and functionalized chains are all hydrocarbon molecules (e.g., surfactant is a C12 linear chain, matrix is a 100,000 Da molecular weight polyethylene, and functionalized chain is a shorter polyethylene molecule with one grafted maleic group). The nonzero interaction parameter between voids and hydrocarbon monomers reflects the nonzero surface tension of polyethylene. The interaction parameter between the clay surface and the hydrocarbon monomers, $\chi_{\alpha c} = 1.0$ ($\alpha = G, F, A$), reflects a very strong incompatibility between the nonpolar polymers and

Table 1 Flory–Huggins interaction parameters used in the calculation

	G	F	A	S	V
Grafted (G)	0.0	0.0	0.0	0.0	1.0
Free matrix (F)	0.0	0.0	0.0	0.0	1.0
Active (A)	0.0	0.0	0.0	0.0	1.0
Sticker (S)	0.0	0.0	0.0	0.0	1.0
Void (V)	1.0	1.0	1.0	1.0	0.0

the polar clay surface. The interaction parameter between the clay surface and the voids—related to the surface tension of the bare clay—was set to 2.0 to reflect the fact that the surface energy of the clay should be much higher than that of the polymers. Finally, the interaction parameter between the stickers and the clay surface, χ_{SC}, was varied to study the influence of the adhesion strength on the phase behavior. (The range of χ_{SC} investigated here, between 0 and -100, roughly corresponds to sticker–surface adhesion energy, $\varepsilon = -\chi_{SC}/6$, being bracketed between 0 and 10 kcal/mol, which is typical for hydrogen-bonding interactions.) We also varied the volume (or weight) fraction of the active chains. Finally, all the calculations were repeated for two densities: $\phi_v^b = 0$ (incompressible melt, the model equivalent to earlier studies of Balazs et al.) and $\phi_v^b = 0.4$ (compressible melt). The length of the grafted chains, $N_{gr} = 5$, and the grafting density, $\rho_{gr} = 0.2$, were chosen to match the earlier study of Ginzburg and Balazs (2000). (One difference between the current study and that of Ginzburg and Balazs (2000) is that in that earlier study, Flory–Huggins parameters between the clay and the polymers were set to zero.)

In Figure 11, we plot the calculated free energies, $f(H)$, for several values of χ_{SC}, while keeping the active chain weight fraction constant at 0.05 (same as in the study by Ginzburg and Balazs, 2000). In all cases, the dashed lines correspond to the incompressible model, and the solid lines

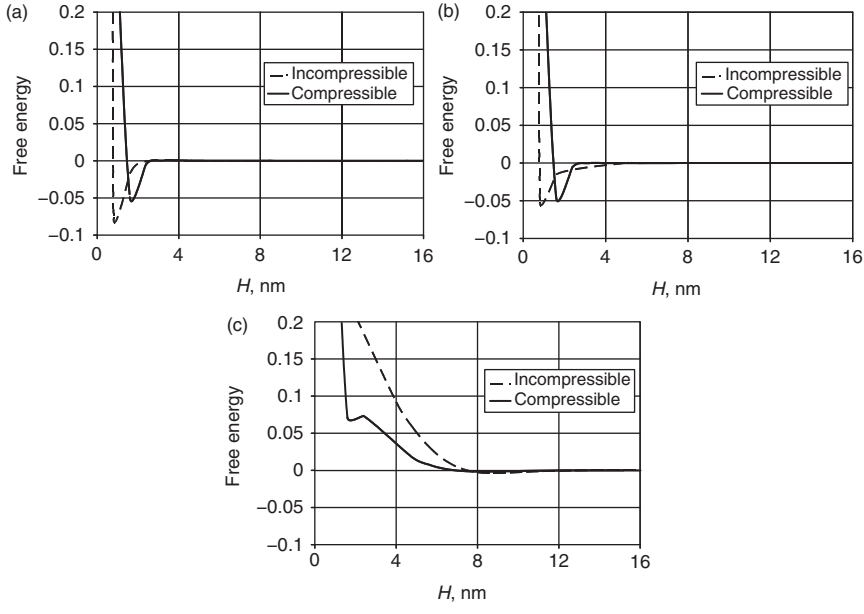

Figure 11 Calculated free energy (per unit area) profiles based on compressible (solid) and incompressible (dashed) lattice SCFT approaches: (a) $\chi_{SC} = 0$; (b) $\chi_{SC} = -48$; (c) $\chi_{SC} = -96$.

are compressible model calculations. We can now carefully examine some of the results.

At low adhesion strength between the sticker and the clay (Figure 11a and b), the free energy has a deep, sharp minimum at small separation. Note that for the incompressible system, this minimum corresponds to the gallery which is "completely closed" and, thus, the plate separation is the same as for the neat organoclay ("immiscible morphology"). For the compressible system, the gallery opens up slightly (the increase in the gallery height is approximately 0.8–1 nm), and the structure that forms is now likely to be interpreted as "intercalated."

For the system with very high adhesion strength between the clay and the stickers, the favorable enthalpy of the sticker–clay interaction dominates the unfavorable entropic contributions. Accordingly (Figure 11c), the composite now becomes exfoliated, as demonstrated by both compressible and incompressible models. Interestingly, within the compressible model, the old minimum at $H \sim 1.6$–2 nm has not disappeared completely, indicating the presence of a metastable intercalated morphology.

What is the origin of this minimum? To understand that, we examined in more detail the case of $\chi_{SC} = -84$. Its compressible free energy profile is shown in Figure 12a, once again indicating the presence of a well-defined minimum at small separations. In Figure 12b, we plot the dependence of polymer density (sum of the volume fractions of all components except for voids) in the gallery on the gallery height. It can be seen that the free energy minimum coincides with the density minimum. Thus, the voids are the first to intercalate the gallery—this initial expansion simply because of the density reduction inside the gallery takes place even before the sticker attachment. The analysis of density profiles at different gallery heights helps understand this. At small separations (Figure 13a), the gallery is penetrated by some active chains, but their amount is relatively low, while the fraction of voids is slightly larger than in the bulk. The grafted chains form strongly overlapping brushes. At intermediate separations (Figure 13b), the brushes no longer overlap, and some matrix chains begin to penetrate the gallery, although end-functionalized chains still account for the majority of the intra-gallery polymer. Finally, at large separations (gallery height much greater than radius of gyration of the active chains), the composition in the center of the gallery is close to that of the bulk polymer, while near the surfaces there is excess of active chains (Figure 13c).

The above discussion centered on a single active chain weight fraction $x = 5$ wt.%. We calculated free energy profiles as function of χ_{SC} for several polymer compositions, varying the active chain content from 0 to 100%. The resulting phase diagram is shown in Figure 14. It can be seen that according to the "compressible" model, the range where intercalated structures could be found has dramatically expanded. Basically, the "initial" intercalation occurs when the plates are separated only slightly,

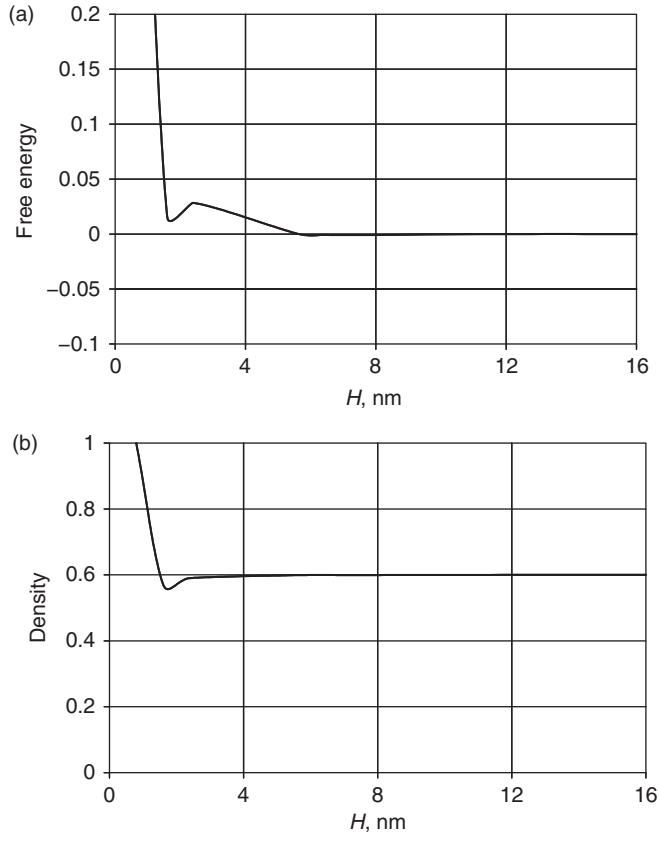

Figure 12 Free energy per unit area (a) and overall polymer density (b) as a function of the gallery height H for the $\chi_{SC} = -84$ system. Calculations are based on the compressible lattice SCFT model.

and the "voids" enter the gallery, thereby substantially decreasing the density of the grafted surfactant. The amount of active polymer entering the gallery is still relatively low. As the gallery height is increased further, the addition of the active chains requires that density go up, thus resulting in the loss of translational entropy for the "voids" (alternatively, this could be thought of simply as additional entropic penalty for higher polymer density). This increase in the free energy could overcome the enthalpic gain from adding a few "stickers" attached to the clay surfaces. Only when the separation is increased substantially, and the number of "stickers" attached to the surface becomes sufficiently high, free energy can decrease to its global minimum.

The above predictions are certainly dependent on the choices of the Flory–Huggins interaction parameters, relative molecular weights of

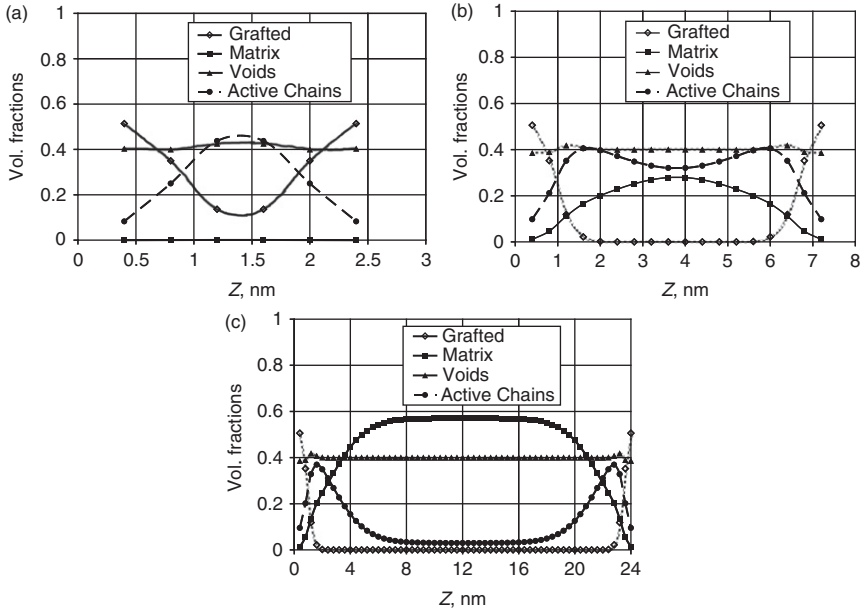

Figure 13 Calculated density profiles for the $\chi_{SC} = -84$ system at various gallery heights H: (a) $H = 2.4$ nm (6 lattice units); (b) $H = 7.2$ nm (18 lattice units); (c) $H = 24$ nm (60 lattice units).

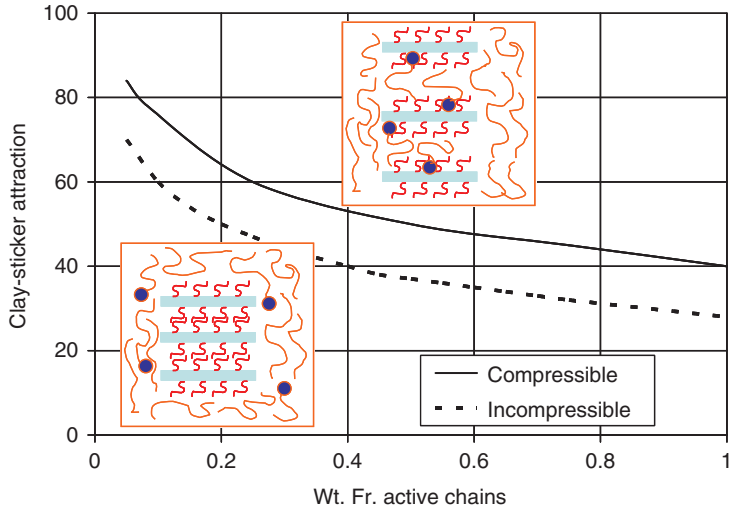

Figure 14 Calculated nanocomposite phase diagram (in the limit of small organoclay loadings). Solid line is the phase boundary between weakly intercalated stacks and partially exfoliated, partially intercalated phase, as calculated using compressible SCFT. Dashed line is the phase boundary between immiscible and exfoliated phases, as calculated by incompressible SCFT.

matrix and sticker chains, matrix polymer density, etc. Even so, the main predictions of the "compressible model"—the shifting of the global free energy minimum toward higher H for the "immiscible" systems and the persistence of the metastable small-H local free energy minimum for the "exfoliated" systems—appear to be universal and robust, at least within the parameter space investigated here.

What are the practical implications of this new model? First, it suggests that intercalated morphologies should be observed, indeed, for majority of nanocomposites. In fact, it is likely that in the melt, almost all nanocomposites exhibit gallery expansion compared to the room-temperature organoclays (see, e.g., Jacobs et al., 2006; Vaia et al., 1994). As nanocomposite is cooled down from the melt to room temperature, the average gallery spacing could shrink back or stay expanded, depending on various kinetic factors. Second, it suggests caution in assuming that intercalated structures must lead to physical or mechanical property improvements. If intercalation proceeds because of the "frozen" density reduction in the galleries, rather than because of the true incorporation of the matrix polymer, the interface between clay and polymer will remain weak, and it would likely adversely impact properties such as toughness. Finally, it is important to note that even for the supposedly exfoliated nanocomposites, the presence of a local free energy minimum means that there is a strong barrier to exfoliation. As discussed by Ginzburg, Gendelman, and Manevitch (Balazs et al., 2008; Gendelman et al., 2003; Ginzburg et al., 2001), if the free energy profile has a double-well structure, the transition from intercalated to exfoliated morphology takes place only when a sufficiently strong shear force is applied to overcome the barrier. The transition would occur via a so-called "kink" mechanism, and the kink could appear if—and only if—the clay stack is subjected to fairly large shear forces. Thus, it is easy to understand why—even if thermodynamically the nanocomposite should be exfoliated—a large fraction of the clay platelets still remains in the metastable, intercalated state.

Yet another implication of the model—and a potentially testable prediction—is that all other things being equal, one could find a higher degree of intercalation in nanocomposites with lower-density matrix polymers, compared to ones with higher density. We are not aware of experimental studies directly testing this proposition (although studies by Vaia and coworkers (1994; Jacobs et al., 2006) appear to provide indirect evidence, as discussed above); we hope that our theoretical analysis would stimulate new investigation in this direction.

4. SUMMARY AND OUTLOOK

In this chapter, we described the application of mesoscale field-based theories (iSAFT and SCFT) to describe polymer-mediated interaction

between two brush-covered flat surfaces. This is a problem that is critical to the successful preparation of polymer–inorganic nanocomposites. While thermodynamics of particles in the polymer matrix is not the only issue determining nanocomposite morphology (dynamics of polymer intercalation and rheology of the particle-filled melt are extremely important as well), its understanding is necessary to properly design a formulation that could potentially lead to the exfoliated and dispersed nanocomposite. That (exfoliation and dispersion) is, in turn, necessary to achieve the desired improvement in mechanical and physical properties.

Of course, nanocomposites are not the only area where mesoscale theories are being used to predict nanostructure and morphology. Other applications include—but are not limited to—block copolymer-based materials, surfactant and lipid liquid crystalline phases, micro-encapsulation of drugs and other actives, and phase behavior of polymer blends and solutions. In all these areas, mesoscale models are utilized to describe—qualitatively and often semi-quantitatively—how the structure of each component and the overall formulation influence the formation of the nanoscale morphology.

Despite all the successes of mesoscale theories, there are some limitations, such as the following:

- Determination of various interaction parameters is difficult and sometimes arbitrary.
- It is still very difficult to properly account for electrostatic interactions (there have been some attempts to incorporate electrostatics into SCFT (Popov et al., 2007), but their applicability is still rather limited).
- It is still difficult to apply mesoscale theories to describe aqueous solutions, as the description of hydrogen bonding is not yet very successful.

We anticipate that as these mesoscale approaches are developed and their shortcomings are overcome, their application in chemical engineering will become more and more widespread. Eventually, it is our expectation that the use of these models will become as common as the use of continuum hydrodynamics and quantum chemistry models is today.

ACKNOWLEDGMENT

WGC and SJ acknowledge financial support provided by the Robert A. Welch Foundation (Grant No. C1241) and by the National Science Foundation (CBET-0756166).

REFERENCES

Alexandre, M., and Dubois, P. *Mater. Sci. Eng. R Rep.* **28**(1–2), 1–63 (2000).

Balazs, A. C., Bicerano, J., and Ginzburg, V. V., Polyolefins/clay nanocomposites: Theory and simulation, *in* "Polyolefin Composites" (D. Nwabunma, and T. Kyu, Eds.). Wiley, Chichester, UK (2008).

Balazs, A. C., Ginzburg, V. V., Lyatskaya, Y., Singh, C., and Zhulina, E., Modeling the phase behavior of polymer–clay nanocomposites, *in* "Polymer–Clay Nanocomposites" (T. Pinnavaia, and G. Beall, Eds.), Wiley, Chichester, UK (2000).
Balazs, A. C., Singh, C., and Zhulina, E. *Macromolecules* **31**(23), 8370–8381 (1998).
Balazs, A. C., Singh, C., and Zhulina, E. *Macromolecules* **31**, 8370 (1998).
Balazs, A. C., Singh, C., Zhulina, E., and Lyatskaya, Y. *Acc. Chem. Res*. **32**(8), 651–657 (1999).
Balazs, A. C., Singh, C., Zhulina, E., and Lyatskaya, Y. *Acc. Chem. Res*. **32**, 651 (1999).
Baschnagel, J., Binder, K., Doruker, P., Gusev, A., Hahn, O., Kremer, K., Mattice, W., Mueller-Plathe, F., Murat, M., Paul, W., Santos, S., Suter, U. W., and Tries, V. *Adv. Polym. Sci*. **152**, 41–156 (2000).
Bates, F. S., and Fredrickson, G. H. *Phys. Today* **52**(2), 32–38 (1999).
Beyer, F. L., Beck Tan, N. C., Dasgupta, A., and Galvin, M. E. *Chem. Mater*. **14**, 2983 (2002).
Bymaster, A. and Chapman, W.G., *J. Phys. Chem*. B, submitted (2010).
Chandler, D., McCoy, J. D., and Singer, S. J. *J. Chem. Phys*. **85**(10), 5977–5982 (1986).
Chapman, W.G., Theory and Simulation of Associating Liquid Mixtures. Ph.D. thesis Cornell University (1988).
Chapman, W. G., Gubbins, K. E., Jackson, G., and Radosz, M. *Fluid Phase Equilib*. **52**, 31–38 (1989).
Chapman, W. G., Gubbins, K. E., Jackson, G., and Radosz, M. *Ind. Eng. Chem. Res*. **29**(8), 1709–1721 (1990).
Chapman, W. G., Gubbins, K. E., Joslin, C. G., and Gray, C. G. *Fluid Phase Equilib*. **29**, 337–346 (1986).
Davis, H. T., "Statistical Mechanics of Phases, Interfaces and Thin Films". VCH, New York (1997).
Dominik, A., Tripathi, S., and Chapman, W. G. *Ind. Eng. Chem. Res*. **45**(20), 6785–6792 (2006).
Evans, R., *in* "Density Functionals in the Theory of Non-uniform Fluids". (D. Henderson Ed.). Fundamentals of Inhomogeneous Fluids, pp. 85–175. Marcel Dekker, New York. 85–175 (1992).
Ebner, C., Saam, W. F., and Stroud, D. *Phys. Rev. A* **14**(6), 2264 LP–2273 (1976).
Evans, R., and Marconi, U. M.B. *J. Chem. Phys*. **86**(12), 7138–7148 (1987).
Ferreira, P. G., Ajdari, A., and Leibler, L. *Macromolecules* **31**(12), 3994–4003 (1998).
Gendelman, O. V., Manevitch, L. I., and Manevitch, O. L. *J. Chem. Phys*. **119**, 1066 (2003).
Giannelis, E. P., Krishnamoorti, R., and Manias, E., Polymer-silicate nanocomposites: Model systems for confined polymers and polymer brushes, *in* "Polymers in Confined Environments", pp. 107–147. Springerg, Berlin (1999).
Ginzburg, V. V., and Balazs, A. C. *Adv. Mater*. **12**, 1805 (2000).
Ginzburg, V. V., Gendelman, O. V., and Manevitch, L. I. *Phys. Rev. Lett*. **86**, 5073 (2001).
Ginzburg, V. V., Weinhold, J. D., Jog, P. K., and Srivastava, R. *Macromolecules* **42**(22), 9089–9095 (2009).
Grest, G. S., and Murat, M. *Macromolecules* **26**(12), 3108–3117 (1993).
Gross, J., and Sadowski, G. *Ind. Eng. Chem. Res*. **41**(5), 1084–1093 (2002).
Ginzburg, V. V., Singh, C., and Balazs, A. C. *Macromolecules* **33**, 1089 (2000).
Gross, J., Spuhl, O., Tumakaka, F., and Sadowski, G. *Ind. Eng. Chem. Res*. **42**(6), 1266–1274 (2003).
Hansen, J. P., and McDonald, I. R., "Theory of Simple Fluids". Academic Press, New York (1986).
Hasegawa, N., Okamoto, H., Kawasumi, M., Kato, M., Tsukigase, A., and Usuki, A. *Macromol. Mater. Eng*. **280/281**, 76 (2000).
Hohenberg, P., and Kohn, W. *Phys. Rev*. **136**(3B), B864 LP–B871 LP (1964).
Jackson, G., Chapman, W. G., and Gubbins, K. E., Proceedings, Annual Convention—Gas Processors Association, **67**, pp. 242–250 (1988).

Jain, S., Ginzburg, V. V., Jog, P., Weinhold, J., Srivastava, R., and Chapman, W. G. *J. Chem. Phys*. **131**(4), 044908 (2009).
Jacobs, J. D., Koerner, H., Heinz, H., Farmer, B. L., Mirau, P., Garrett, P. H., and Vaia, R. A. *J. Phys. Chem. B* **110**, 20143 (2006).
Jain, S., Dominik, A., and Chapman, W. G. *J. Chem. Phys*. **127**(24), 244904–12 (2007).
Jain, S., Jog, P., Weinhold, J., Srivastava, R., and Chapman, W. G. *J. Chem. Phys*. **128**(15), 154910 (2008).
Joslin, C. G., Gray, C. G., Chapman, W. G., and Gubbins, K. E. *Mol. Phys*. **62**(4), 843–60 (1987).
Kierlik, E., and Rosinberg, M. L. *J. Chem. Phys*. **97**(12), 9222–9239 (1992).
Leibler, L., Ajdari, A., Mourran, A., Coulon, G., and Chatenay, D., "OUMS Conference on Ordering in Macromolecular Systems". Springer, Berlin, Osaka (1994).
Lyatskaya, Y., and Balazs, A. C. *Macromolecules* **31**, 6676 (1998).
Lyatskaya, Y., Gersappe, D., Gross, N. A., and Balazs, A. C. *J. Phys. Chem*. **100**(5), 1449–1458 (1996).
Matsen, M. W., and Bates, F. S. *Macromolecules* **29**(4), 1091–1098 (1996).
Matsen, M. W., and Gardiner, J. M. *J. Chem. Phys*. **115**(6), 2794–2804 (2001).
McCoy, J. D., and Curro, J. G. *J. Chem. Phys*. **122**, 164905–164907 (2005).
Mueller, E. A., and Gubbins, K. E. *Ind. Eng. Chem. Res*. **40**(10), 2193–2211 (2001).
Okada, A., Kawasumi, M., Usuki, A., Kojima, Y., Kurauchi, T., and Kamigaito, O., Synthesis and properties of Nylon-6/clay hybrids, *in* "Polymer Based Molecular Composites, MRS Symposium Proceedings" (D. W. Schaefer, and J. E. Mark Eds.), Vol. 171, pp. 45–50. Materials Research Society, Pittsburgh, PA (1990).
Phan, S., Kierlik, E., Rosinberg, M. L., Yethiraj, A., and Dickman, R. *J. Chem. Phys*. **102**(5), 2141–2150 (1995).
Popov, Y. O., Lee, J., and Fredrickson, G. H. *J. Polym. Sci. B Polym. Phys*. **45**(24), 3223–3230 (2007).
Rosenfeld, Y. *Phys. Rev. Lett*. **63**, 980 (1989).
Scheutjens, J. M.H.M., and Fleer, G. J. *J. Phys. Chem*. **83**, 1619 (1979).
Scheutjens, J. M.H.M., and Fleer, G. J. *J. Phys. Chem*. **84**, 178 (1980).
Schweizer, K. S., and Curro, J. G. *Adv. Chem. Phys*. **98**, 1 (1997).
Segura, C. J., Chapman, W. G., and Shulka, K. P. *Mol. Phys*. **90**(5), 759–771 (1997).
Sinha Ray, S., and Okamoto, M. *Prog. Polym. Sci*. **28**(11), 1539–1641 (2003).
Swain, S. K., and Isayev, A. I. *Polymer* **48**, 281 (2007).
Tripathi, S., Microstructure and Phase Behavior of Inhomogeneous Complex Fluids, Ph.D. thesis, Rice University (2005).
Tripathi, S., and Chapman, W. G. *J. Chem. Phys*. **122**(9), 094506–094511 (2005a).
Tripathi, S., and Chapman, W. G. *Phys. Rev. Lett*. **94**(8), 087801 (2005b).
Tumakaka, F., Gross, J., and Sadowski, G. *Fluid Phase Equilib*. **194-197**, 541–551 (2002).
Vaia, R. A., and Giannelis, E. P. *Macromolecules* **30**(25), 7990–7999 (1997a).
Vaia, R. A., and Giannelis, E. P. *Macromolecules* **30**(25), 8000–8009 (1997b).
Vaia, R. A., Teukolsky, R. K., and Giannelis, E. P. *Chem. Mater*. **6**, 1017 (1994).
Wertheim, M. S. *J. Stat. Phys*. **35**, 19 (1984a).
Wertheim, M. S. *J. Stat. Phys*. **35**, 35 (1984b).
Wertheim, M. S. *J. Stat. Phys*. **42**, 459 (1986a).
Wertheim, M. S. *J. Stat. Phys*. **42**, 477 (1986b).
Wu, J. *AIChE J*. **52**(3), 1169–1193 (2006).
Wu, J., and Li, Z. Annu. *Rev. Phys. Chem*. **58**(1), 85–112 (2007).
Yethiraj, A., "Chemical Applications of Density-Functional Theory" (B. B. Laird, R. B. Ross, and T. Ziegler Eds.), p. 274. American Chemical Society, Washington, DC (1996).
Yethiraj, A. *J. Chem. Phys*. **109**, 3269–3275 (1998).
Yethiraj, A. *Adv. Chem. Phys*. **121**, 89 (2002).
Yu, Y.-X., and Wu, J. *J. Chem. Phys*. **117**(5), 2368–2376 (2002).
Zhulina, E., Singh, C., and Balazs, A. C. *Langmuir* **15**, 3935 (1999).